Eur. Phys. J. Plus (2026) 141:626
https://doi.org/10.1140/epjp/s13360-026-07853-9

THE EUROPEAN PHYSICAL JOURNAL PLUS

Regular Article

Mitigating the phase-mismatch effect in non-resonant four-wave mixing enabled by optimal control

Ning Jia[1], **Hamid R. Hamedi**[2,a], **Jing Qian**[3,4,b]

[1] Public Experiment Center, University of Shanghai for Science and Technology, Shanghai 200093, China
[2] Institute of Theoretical Physics and Astronomy, Vilnius University, Saulėtekio 3, Vilnius LT-10257, Lithuania
[3] Quantum Institute for Light and Atoms, School of Physics, East China Normal University, Shanghai 200062, China
[4] Chongqing Institute of East China Normal University, Chongqing 401120, China

Received: 12 December 2025 / Accepted: 19 May 2026

Abstract Phase-mismatch in nonlinear optical processes can severely limit the propagation and conversion efficiency of light fields. Here, we present an efficient optimal-control strategy to mitigate the detrimental effects of phase-mismatch in an electromagnetically induced transparency based medium via non-resonant four-wave mixing (FWM) process. By applying a set of fixed, linearly modulated coupling fields that induce a dark eigenmode, we globally optimize a single coupling detuning to minimize the spontaneous emission loss, the primary factor limiting conversion efficiency. Our approach outperforms existing FWM schemes by providing stronger robustness against large phase-mismatch variations while maintaining efficient probe-to-signal conversion. These results offer a promising route toward more efficient nonlinear frequency conversion, alleviating the stringent requirement for phase matching in experiments.

1 Introduction

Four-wave mixing (FWM) in double-Λ atomic systems operating under electromagnetically induced transparency (EIT) conditions has attracted considerable interests for quantum frequency conversion and photonic applications [1–5]. In such systems, the formation of a dark state which suppresses spontaneous emission from excited states, enables coherent energy transfer from probe to signal lasers with high conversion efficiency (CE) [6–8]. Exploiting this mechanism, a recent FWM experiment with spatially modulated coupling fields achieved a CE above 43% at an optical depth (OD) of 19 in cold ^{87}Rb atoms, with theoretical predictions reaching 96% if OD is 240 [9]. This outperforms conventional schemes because the system operates in a dark transmission mode, largely minimizing the atomic absorptive loss due to spontaneous emission. However, realizing such spatial modulation typically requires non-collinear laser beam geometries with large separation angles. This configuration inevitably introduces considerable wavevector mismatch, degrades the CE and limits practical applicability. Therefore, the phase-mismatch effect, commonly-existed in complex nonlinear atom-light systems, serves as a major obstacle to the route of efficient frequency conversion [10–12].

So far a variety of strategies have been proposed to mitigate this phase-mismatch, but most of which remain insufficient or experimentally demanding [13–15]. Except for elaborate experimental setups that require multiple precisely aligned pump and seed beams, careful phase-matching control, and atomic-state preparation to maintain coherence [16–19], previous efforts to overcome this issue have shown that one can, for example, create a sufficiently large nonlinear polarization to enable efficient frequency conversion within a single (non-phase-matched) coherence length [20]. In particular, constant two-photon detunings can compensate small phase-mismatches by adjusting the relative phase between probe and coupling fields, but is limited to small, precisely known mismatches.

Despite prior advances, achieving high CE over a broad range of phase-mismatches remains an open challenge. In this work, we propose a globally optimal-control method to mitigate this phase-mismatch effect in a non-resonant FWM system. Numerical optimization is performed using genetic algorithm (GA) method [21] with fine-tuning coupling detuning that varies smoothly in space, while preserving a set of space-delayed coupling fields to minimize atomic spontaneous emission loss, analogously used in Ref. [22]. Our results demonstrate that high-efficiency frequency conversion can be achieved with enhanced robustness against significant phase-mismatch errors. Notably, even modest phase-mismatches—corresponding to small angles between the probe and coupling fields—can noticeably reduce CE in realistic experiments [19]. To illustrate the effectiveness and robustness of our approach, we explore mismatch angles up to $\varphi \approx 8°$ for larger OD, and extend to $\varphi \approx 13.6°$ for moderate OD to intentionally stress-

[a] e-mail: hamid.hamedi@tfai.vu.lt (corresponding author)
[b] e-mail: jqian1982@gmail.com (corresponding author)

Published online: 02 June 2026

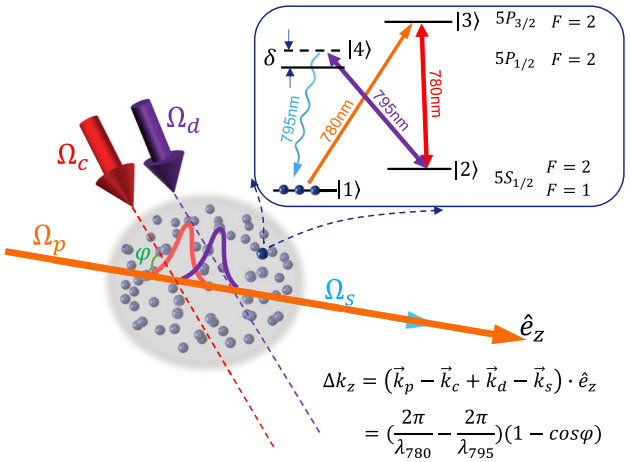

Fig. 1 Restriction by the phase-mismatch effect in a non-resonant double-Λ FWM system [9]. The phase-mismatch term Δk_z, arising from the separated angle φ between the propagation directions of the probe (Ω_p) and coupling ($\Omega_{d,c}$) beams, is detrimental to the generation of signal field (Ω_s). Inset: Schematic level scheme and relevant energy states in ^{87}Rb atoms, with $|1\rangle = |5S_{1/2},\ F=1,\ m_F=0\rangle$, $|2\rangle = |5S_{1/2},\ F=2,\ m_F=0\rangle$, $|3\rangle = |5P_{3/2},\ F=2,\ m_F=+1\rangle$, and $|4\rangle = |5P_{1/2},\ F=2,\ m_F=+1\rangle$, connected by σ^+-polarized fields ($\Delta m_F = +1$) at wavelengths $\lambda_{780} = 780$ nm and $\lambda_{795} = 795$ nm. The quantization axis is chosen along the $+z$-axis propagation direction of the probe and signal fields

test the protocol. This work, therefore, expands the scope of phase-mismatch control by integrating it with a global optimal-control framework, distinguishing it from previous optimization approaches such as Ref. [22], and highlighting its potential for versatile quantum photonic applications [23, 24].

2 Theoretical strategy

The atomic system is of the double-Λ type, consisting of two ground states $|1\rangle$ and $|2\rangle$, and two excited states $|3\rangle$ and $|4\rangle$. When states $|2\rangle$ and $\{|3\rangle,\ |4\rangle\}$ are driven by two strong coupling fields $\Omega_{c,d}$ (with central frequency $\omega_{c,d}$ and wavevector $\vec{k}_{c,d}$), the weak-probe beam Ω_p (central frequency ω_p and wavevector $\vec{k}_p$) driving the transition from $|1\rangle$ to $|3\rangle$ induces a fourth weak signal field Ω_s (with central frequency ω_s and wavevector $\vec{k}_s$), forming a standard FWM process $|1\rangle \rightarrow |3\rangle \rightarrow |2\rangle \rightarrow |4\rangle \rightarrow |1\rangle$ [25], as shown in Fig. 1. The original Hamiltonian of system is ($\hbar = 1$)

$$\begin{aligned}\hat{H} =& \sum_{j=2}^{4} \omega_j |j\rangle\langle j| + \Big(\Omega_p e^{-i\omega_p t}|3\rangle\langle 1| + \Omega_c e^{-i\omega_c t}|3\rangle\langle 2| \\ &+ \Omega_d e^{-i\omega_d t}|4\rangle\langle 2| + \Omega_s e^{-i\omega_s t}|4\rangle\langle 1| + \text{H.c.}\Big),\end{aligned} \tag{1}$$

where $\omega_1 \equiv 0$ sets the energy reference. We first apply the unitary transformation $U = \exp(i\hat{H}_0 t)$ with $\hat{H}_0 = (\omega_p - \omega_c)|2\rangle\langle 2| + \omega_p|3\rangle\langle 3| + (\omega_p - \omega_c + \omega_d)|4\rangle\langle 4|$. Since the energy conserves in the FWM process [26], i.e., $\omega_s = \omega_p - \omega_c + \omega_d$, the rotating-frame Hamiltonian $\tilde{H} = U\hat{H}U^\dagger + i\dot{U}U^\dagger$ can be written as

$$\begin{aligned}\tilde{H} =& \delta_p|3\rangle\langle 3| + (\delta_p - \delta_c)|2\rangle\langle 2| + (\delta_p - \delta_c + \delta_d)|4\rangle\langle 4| \\ &+ \Big(\Omega_p|3\rangle\langle 1| + \Omega_c|3\rangle\langle 2| + \Omega_d|4\rangle\langle 2| + \Omega_s|4\rangle\langle 1| + \text{H.c.}\Big),\end{aligned} \tag{2}$$

with detunings $\delta_p = \omega_3 - \omega_p$, $\delta_c = \omega_3 - \omega_2 - \omega_c$, and $\delta_d = \omega_4 - \omega_2 - \omega_d$. Here, we assume the probe Ω_p and coupling Ω_c fields resonant to their respective transitions ($\delta_p = \delta_c = 0$), and choose $\delta = \delta_d$ (respect to Ω_d) as the only control knob to enhance CE by avoiding the multi-photon destructive interference [27]. Seen from Fig. 1 (inset), we also ignore the small hyperfine energy splitting between ground manifolds focusing on the mismatch error created by two different wavelengths. As a result, the rotating-frame Hamiltonian reduces to

$$\tilde{H} = \delta|4\rangle\langle 4| + \big(\Omega_p|3\rangle\langle 1| + \Omega_c|3\rangle\langle 2| + \Omega_d|4\rangle\langle 2| + \Omega_s|4\rangle\langle 1| + \text{H.c.}\big). \tag{3}$$

The dynamics of system is governed by the density-matrix master equation [28]

$$\frac{\partial \rho}{\partial t} = -i\Big[\tilde{H}, \rho\Big] + \mathcal{L}_d[\rho] + \mathcal{L}_z[\rho], \tag{4}$$

where the Lindblad superoperators are

$$\mathcal{L}_d[\rho] = \sum_{m\in\{1,2\}} \sum_{n\in\{3,4\}} \left(L_{mn}\rho L_{mn}^\dagger - \frac{1}{2}\{L_{mn}^\dagger L_{mn}, \rho\}\right), \tag{5}$$

$$\mathcal{L}_z[\rho] = L_z \rho L_z^\dagger - \frac{1}{2}\{L_z^\dagger L_z, \rho\} \tag{6}$$

The first term $\mathcal{L}_d[\rho]$ accounts for the spontaneous decay from excited states $|n\rangle$ to ground states $|m\rangle$ at rate $L_{mn} = \sqrt{\Gamma_{nm}}|m\rangle\langle n|$, and the second one $L_z = \sqrt{\gamma}(|1\rangle\langle 1| - |2\rangle\langle 2|)$ describes the ground-state dephasing at rate γ. Note that pure dephasing of the excited states $|3\rangle$ and $|4\rangle$ is neglected, since spontaneous emission, characterized by the decay rate Γ, dominates over any residual pure dephasing mechanisms. In contrast, the ground-state coherence is not subject to radiative decay and is, therefore, affected only by residual dephasing processes, which are explicitly included via the rate γ [5].

In order to provide an analytical discussion, we further consider the weak-probe approximation where $\Omega_p \ll \Omega_{c,d}$ is met [29], so atoms will persistently stay in the initial state $|1\rangle$, satisfying $\rho_{11} \approx 1$, $\rho_{jj} \approx 0$ with $j \in (2, 3, 4)$. If the probe or signal fields become sufficiently strong as compared to the coupling fields, this approximation breaks, and one needs to solve the full set of coupled propagation equations involving 16 density-matrix elements $\rho_{ij}(i,\ j = 1, ..., 4)$ [30]. This issue will leave for future studies. Thereby, we retain only the atomic coherence terms associated to the initial state $|1\rangle$, yielding three reduced equations,

$$\frac{\partial}{\partial t}\rho_{41} = i(\Omega_s + \Omega_d \rho_{21}) + \left(i\delta - \frac{\Gamma + \gamma}{2}\right)\rho_{41}, \tag{7a}$$

$$\frac{\partial}{\partial t}\rho_{31} = i\left(\Omega_p + \Omega_c \rho_{21}\right) - \frac{\Gamma + \gamma}{2}\rho_{31}, \tag{7b}$$

$$\frac{\partial}{\partial t}\rho_{21} = i\left(\Omega_c^* \rho_{31} + \Omega_d^* \rho_{41}\right) - \gamma \rho_{21}, \tag{7c}$$

where we assume $\Gamma_{nm} = \Gamma/2$ for simplicity because the hyperfine excited or ground energy levels often share similar properties, see caption of Fig. 1. Moreover, to obtain an explicit interpretation under the perfect EIT condition [31], we adopt a zero dephasing rate ($\gamma = 0$) whereas this effect will be considered in the later numerical calculations. Next, by using the steady-state assumption, we can directly solve the atomic coherence related to the propagation of probe and signal fields

$$\rho_{31} = i\left(-|\Omega_d|^2 \Omega_p - \Omega_d^* \Omega_c \Omega_s\right)/D, \tag{8}$$

$$\rho_{41} = i\left(-\Omega_c^* \Omega_d \Omega_p + |\Omega_c|^2 \Omega_s\right)/D, \tag{9}$$

where $D = (\Gamma - 2i\delta)|\Omega_c|^2 + \Gamma|\Omega_d|^2$.

In our setup, the probe and signal fields propagate along the z-axis, while the two control fields co-propagate at the same angle φ with respect to this axis. For concreteness, we assume these tilts lie in the x-z plane, yielding wave vectors $\vec{k}_{c,d} = k_{c,d}(\cos\varphi\,\hat{z} + \sin\varphi\,\hat{x})$. The longitudinal phase-mismatch is then $\Delta k_z = k_p - k_c\cos\varphi + k_d\cos\varphi - k_s$. Given that $k_p = k_c = 2\pi/\lambda_{780}$ and $k_d = k_s = 2\pi/\lambda_{795}$, this expression simplifies to

$$\Delta k_z = \left(\frac{2\pi}{\lambda_{780}} - \frac{2\pi}{\lambda_{795}}\right)(1 - \cos\varphi). \tag{10}$$

representing the phase-mismatch strength in our scheme.

To describe the propagation of the probe (Ω_p) and generated signal (Ω_s) fields in the atomic medium, we use the Maxwell–Bloch equations derived from Maxwell's equations under the slowly varying envelope approximation [32]:

$$\frac{\partial \Omega_p}{\partial z} + \frac{1}{c}\frac{\partial \Omega_p}{\partial t} = i\frac{\alpha_p \Gamma}{2L}\rho_{31}, \qquad \frac{\partial \Omega_s}{\partial z} + \frac{1}{c}\frac{\partial \Omega_s}{\partial t} + i\Delta k_z \Omega_s = i\frac{\alpha_s \Gamma}{2L}\rho_{41}, \tag{11}$$

Here, L is the medium length and we have ignored the diffraction terms ($\nabla_\perp^2$) since the universal Rayleigh length $\pi\omega_0^2/\lambda$ is much larger than the propagation length L. E.g., when $L = 3.5$ mm in our system, $\omega_0 = 140\ \mu$m and $\lambda = 795$ nm yield $\pi\omega_0^2/\lambda \approx 7.8$ cm $\gg L$. Besides we define a dimensionless mismatch parameter $\kappa = \Delta k_z L$, scaled such that $\kappa \in [0, 5]$, corresponding to a relatively small angle $\varphi \lesssim 8°$ for $L = 3.5$ mm [33]. α_p and α_s are the ODs with respect to the probe and signal transitions and we take $\alpha_p = \alpha_s = \alpha$ for simplicity. Within the steady-state regime, the field envelopes vary slowly compared to the optical period and atomic relaxation times, allowing us to safely neglect the time-derivative terms $\propto \partial/\partial t$. The term $i\Delta k_z$ accounts for longitudinal phase-mismatch in FWM, introducing a spatial phase variation that can severely reduce the CE.

By inserting Eqs.(8) and (9) into the propagation Eq. (11) without time-derivative terms, the system forms as Schrödinger-like coupled equations (L serves as a length unit)

$$i\frac{\partial}{\partial z}\begin{pmatrix}\Omega_p \\ \Omega_s\end{pmatrix} = \mathcal{M}\begin{pmatrix}\Omega_p \\ \Omega_s\end{pmatrix} \tag{12}$$

where

$$\mathcal{M} = \begin{pmatrix}\zeta \sin^2\theta & -\zeta\sin(2\theta)/2 \\ -\zeta\sin(2\theta)/2 & \zeta\cos^2\theta + \kappa\end{pmatrix} \tag{13}$$

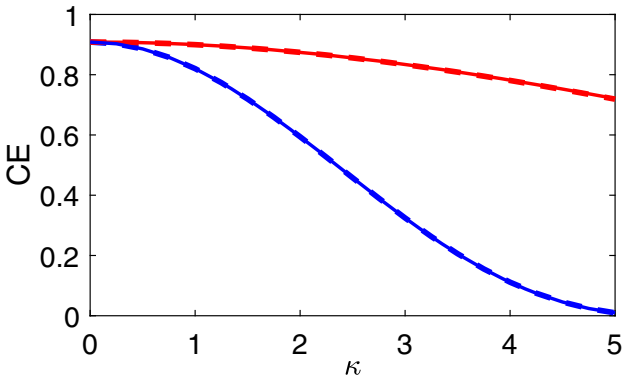

Fig. 2 Comparison of CE as a function of phase-mismatch κ, with optimal parameters ($\theta_{\rm opt}(\kappa)$, $\delta_{\rm opt}(\kappa)$) (red, Protocol I) and fixed parameters ($\theta_{\rm opt}(0)$, $\delta_{\rm opt}(0)$) (blue). The realistic behavior solved from Eq. (4) is shown by the solid lines, and the theoretical predictions shown by dashed lines are plotted using the computed CE function in Eq. (15). Other parameters are $\alpha = 200$, $\gamma = 0$, $\Omega_p = 0.03$, $\Omega_d = 1.5$, $\Omega_c = \Omega_d \cot\theta$ is κ-dependent and Γ serves as the frequency unit and L serves as the length unit throughout

with the coefficient ζ given by

$$\zeta = \frac{\alpha\Gamma}{2}\left(\frac{2\delta\cos^2\theta - i\Gamma}{\Gamma^2 + 4\delta^2\cos^4\theta}\right). \tag{14}$$

Remarkably, we define a new ratio $\Omega_c/\Omega_d = \cot\theta$, indicating that propagation depends only on the ratio of the two coupling fields rather than their absolute values. In principle, the shape of Ω_c and Ω_d can be arbitrary in space, provided that the dark eigenmode ψ_D is maintained (see Eq. 18). Additionally, we find the spontaneous decay loss, incorporated through the non-Hermitian matrix $\mathcal{M}$ via the imaginary part of ζ, scales as $\propto e^{-\alpha/2}$ for both Ω_p and Ω_s, decreasing exponentially if α increases. Hence, a dense atomic medium with a large α (≈ 500) can achieve near-unity signal conversion [34]. In what follows, depending on optimal-control tools we focus on achieving a high CE by reducing the spontaneous decay loss, even under the existence of a large phase-mismatch.

3 Results and discussion

3.1 Protocol I: constant-optimization

From the coupled propagation equation in Eq. 12, if all parameters are time-independent, we can analytically solve CE which quantifies the performance of signal transmission, as

$$\mathrm{CE} = \frac{|\Omega_s(z=1)|^2}{|\Omega_{p0}|^2} = \frac{|\zeta\sin(2\theta)|^2}{4|\lambda_+ - \lambda_-|^2}|e^{\lambda_+} - e^{\lambda_-}|^2 \tag{15}$$

where $\lambda_\pm = \frac{1}{2}\left(\zeta + \kappa \pm \sqrt{\zeta^2 + \kappa^2 + 2\kappa\zeta\cos(2\theta)}\right)$ are the eigenvalues of $\mathcal{M}$. To maximize CE, we first introduce the constant-optimization method denoted as Protocol I, where the diagonal energy shift of matrix $\mathcal{M}$ is set to vanish, and a π-pulse coupling is enforced via the relationship $|\zeta\sin(2\theta)|z = \pi$ (see appendix A). Finally, we arrive at a set of optimal κ-dependent constants ($\theta_{\rm opt}$, $\delta_{\rm opt}$) for a best CE:

$$\theta_{\rm opt} = \frac{\pi}{4} + \frac{1}{2}\arctan(\kappa/\pi), \qquad \delta_{\rm opt} = \frac{\alpha}{2\pi^2}(\kappa + \sqrt{\kappa^2 + \pi^2}). \tag{16}$$

In the ideal phase-matching case, i.e., $\kappa = 0$, one gets ($\theta_{\rm opt}$, $\delta_{\rm opt}$) = ($\frac{\pi}{4}$, $\frac{\alpha}{2\pi}$) arising the maximal CE value,

$$\mathrm{CE} = \frac{1}{4}(1 + e^{-\frac{2\pi^2}{\alpha}})^2. \tag{17}$$

At a large OD, e.g., $\alpha = 200$, it gives CE=0.911, comparable to other FWM protocols [35]. For a moderate OD ($\alpha = 50$), CE still preserves at 0.700. However, any nonzero phase-mismatch $\kappa \neq 0$ would be strongly detrimental to the high-efficiency generation of FWM signals.

Figure 2 shows the CE impacted by κ in a double-Λ FWM system. If the parameters are fixed at their optimal phase-matched values (θ, δ) = ($\frac{\pi}{4}$, $\frac{\alpha}{2\pi}$) (blue curves), CE drops rapidly with increasing κ, reaching CE ≈ 0.01 at $\kappa = 5$. In contrast, the analytic solution of Eq.(16) developed in Protocol I (red curves) yields substantial improvement: for any given κ, setting the coupling fields in the ratio $\Omega_c = \Omega_d \cot\theta_{\rm opt}$ together with the κ-dependent detuning $\delta_{\rm opt}$ can significantly enhance CE, reaching 0.72 for $\kappa = 5$. The full numerical solutions (solid) based on the density-matrix evolution (4) perfectly validate the scheme accuracy (dashed). Thus, this constant-optimization strategy can partly compensate for the phase-mismatch at the cost of a precise knowledge of κ, which is unrealistic in experiments, motivating a more robust space-dependent optimization.

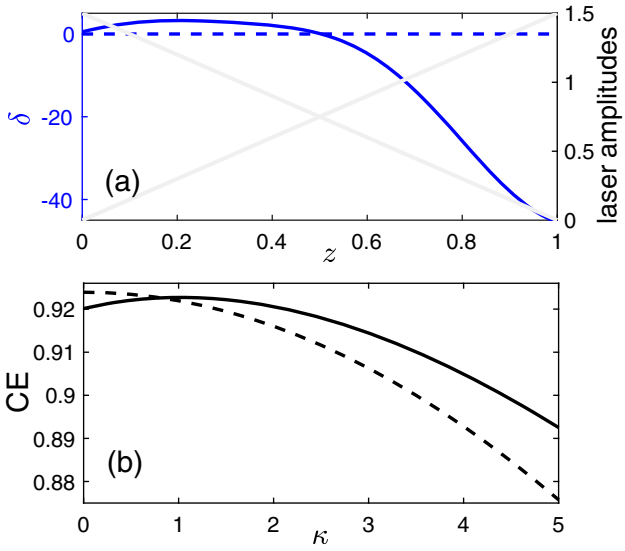

Fig. 3 Performance of the FWM scheme as a function of phase-mismatch κ under different optimized waveforms $\delta(z)$. The curves comparably represent the cases of $\delta(z) = 0$ (Protocol II, dashed) and $\delta = \delta(z)$ (Protocol III, solid) where optimized coefficients are (a_0, a_1, a_2, a_3, b_1, b_2, b_3) = (−13.55, 20.15, 6.17, −8.93, −0.91, 2.86, 1.45). **a** and **b** corresponds to the detuning waveforms and the calculated CE values, respectively. The light gray curves in **a** indicate the unchanged adiabatic amplitudes of $\Omega_c(z)$ and $\Omega_d(z)$ behaving as a space-delayed pattern. Relevant parameters are $\alpha = 200$, $\Omega_p = 0.03$, $\gamma = 10^{-4}$, $\Omega_{c0} = \Omega_{d0} = 1.5$

3.2 Protocols II and III: Space-dependent optimization

To further improve the CE, especially in the case of large phase-mismatch, we introduce two orthogonal base vectors

$$\psi_D = (\cos\theta,\ \sin\theta)^T, \qquad \psi_B = (\sin\theta,\ -\cos\theta)^T, \tag{18}$$

which coincide with the eigenstates of $\mathcal{M}$ for $\kappa = 0$, corresponding to eigenvalues $\lambda_+ = 0$ and $\lambda_- = \zeta$. In the phase-matched case, ψ_D forms like a dark state, fully protected from spontaneous dissipation arising from the imaginary part of ζ. The adiabaticity of this dark-state improves with optical depth α, since a larger α increases the adiabatic energy gap ($\propto \zeta$) relative to nonadiabatic couplings, leading to higher CE. Ideally, with $\theta(z = 0) = 0$, the system can adiabatically evolve along the dark state ψ_D to achieve a complete transfer from Ω_p to Ω_s at $z = 1$, requiring $\theta(z = 1) = \pi/2$. To test the above adiabatic control of $\theta(z)$, we introduce spatially varying amplitudes for the two coupling fields, analogous to the counter-intuitive delayed pulse sequence used in adiabatic passage [36]. Here, $\Omega_{c,d}(z)$ are simply linearly modulated at lower technical cost, following the implementation in [37]

$$\Omega_c(z) = \Omega_{c0}(1 - z), \qquad \Omega_d(z) = \Omega_{d0} z, \tag{19}$$

where Ω_{c0}, Ω_{d0} denote the maximal amplitudes. This configuration allows global optimization to be performed solely through the detuning function $\delta(z)$, while maintaining the adiabatic evolution along the dark state. The spatially waveform of detunings can be implemented by applying an additional Stark field [38] or using magnetic-field-gradient modulation [39]. Notably, the detuning waveform required to achieve high CE is not unique, providing a degree of freedom that can be exploited either to maximize the average CE over a broad range of κ or to optimize CE for a specific large κ (see Sec. 4).

We utilize a numerical GA to determine an optimal waveform $\delta(z)$ that can achieve a higher CE even for relatively large κ values. Taking the average value $F = \sum_{i=1}^{N} \mathrm{CE}(\kappa_i)/N$ as the target we minimize the cost function described by $1 - F$ under sufficient samplings $N = 20$ for $\kappa_i = i/4$, $i = 0, \ldots, N$. We assume the Fourier series form

$$\delta(z) = a_0 + \sum_{n=1}^{3} [a_n \cos(n\pi z) + b_n \sin(n\pi z)]. \tag{20}$$

The detuning waveform is a smooth function in space, facilitating experimental implementation [40]. Note that the coupling amplitudes $\Omega_{c,d}(z)$ are kept unchanged as linear modulation in Protocol II and III.

To demonstrate the improved robustness of FWM protocol against the phase-mismatch effect, we first calculate the CE without optimization by choosing $\delta = 0$ labeled as Protocol II, an un-optimized dark-State case. Excitingly, thanks to the presence of a dark mode ψ_D that adiabatically protects the system from spontaneous loss, the CE values displayed in Fig. 3b by the dashed line can achieve a dramatically increased insensitivity to κ. Even at $\kappa = 5$, the CE remains as high as 0.876, outperforming the maximum ~ 0.72 achieved in Protocol I (see Fig. 2). As turning to Protocol III with an optimized detuning $\delta(z)$, labeled by the solid line, we can obtain stronger robustness against the change of κ. See Fig. 3b, the CE increases to 0.893 for $\kappa = 5$, though at the cost of slightly reduced CE values in the regime of small mismatch values $\kappa \leq 1$. Because our numerical algorithm requires the maximization of average CE value within a broad range $\kappa \in [0, 5]$, it tends to improve the overall insensitivity of scheme performance to the phase-mismatch effect. Specifically, in Protocol III, the optimized $\delta(z)$ function needs to be far from resonance after the adiabatic transfer at $\Omega_c = \Omega_d$, aiming to compensate for the large phase-mismatch κ by employing a largely negative detuning δ ($\approx -45.5\Gamma$) see Fig. 3a. The large magnitude $|\delta(z)|$ suppresses the imaginary part of the effective coupling, $\mathrm{Im}(\zeta) \propto 1/(1 + 4\delta^2 \cos^4\theta)$, thereby

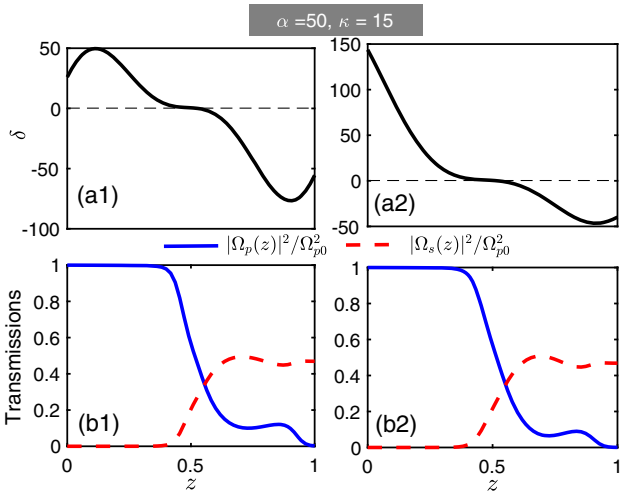

Fig. 4 (a1–2) The optimized waveforms of coupling detuning function. (a1) $\delta(z)$ takes the Fourier series form with coefficients (a_0, a_1, a_2, a_3, b_1, b_2, b_3)=(−1.73,−2.32,−9.08,−13.04,67.86,43.09,1.74). (a2) A different waveform uses Bernstein polynomial where $\delta(z) = \sum_{n=0}^{7} a_n C_7^n z^n (1-z)^{7-n}$ with coefficients (a_0, a_1, a_2, ..., a_7)=(143.76,71.73,−42.35,−53.98,111.60,−59.90,−59.94,−39.85). Here, C_7^n denotes the binomial coefficient. (b1-2) The corresponding transmissions of the probe (solid) and signal (dashed) fields. Here $\alpha = 50$, $\kappa = 15$ and other parameters are the same as in Fig. 3

reducing absorptive loss from the excited states. The negative value and spatial shape of $\delta(z)$ together tailor the dispersive contribution $\mathrm{Re}(\zeta(z))$ so that its integral across the medium length compensates the accumulated phase-mismatch $\Delta k_z L$.

4 Mitigating larger phase-mismatch

In Protocol III, we prove that the spontaneous decay loss due to a finite OD can be decreased by applying an off-resonant detuning modulation. A large negative detuning can also mitigate the significant (positive) phase-mismatch effect in practice. A natural question at this stage arises, whether such space-dependent optimal control of $\delta(z)$ can further improve FWM performance under larger phase-mismatch and moderate OD. This extreme mismatch case, though beyond typical experimental conditions, is intentionally considered to highlight the robustness and potential of the proposed protocol under demanding scenarios. To address this, we examine the CE at $\kappa = 15$ (corresponding to a separation angle $\varphi \approx 13.6°$) with $\alpha = 50$. This choice only gives CE ≈ 0.019 based on Protocol I with optimal constants $(\theta_{\mathrm{opt}}, \delta_{\mathrm{opt}}) = (0.467\pi, 76.82)$. Switching to Protocol II improves CE to 0.132, but the simple spatial-light modulation remains insufficient to overcome the severe energy loss caused by large phase-mismatch. In addition, note that the optical depth is related to measurable quantities through $\alpha = n\sigma L$, where n, σ, L present the atomic density, the absorption cross section and medium length, respectively. Accordingly, if $\alpha \leq 200$ and $\sigma \sim 10^{-9}$ cm^2, the atomic density requires $n \approx 10^{11}$ cm^{-3} accessible by trapping atoms in standard optical traps [41, 42].

In order to achieve a highly efficient conversion for larger mismatch strength in a more practical setting, Protocol III employs GA to search for an optimized detuning waveform $\delta(z)$ at a specific mismatch value $\kappa = 15$, using $1 - \mathrm{CE}(\kappa = 15)$ as the cost function. This ensures maximization of CE around the targeted large phase-mismatch. Note that this may not be the best optimized waveform over the whole range $\kappa \in [0, 15)$. The resulting optimized waveforms of $\delta(z)$ are plotted in Fig. 4. For comparison, we also employ the Bernstein polynomial as an alternative choice [43]. As observed in Fig. 4a1 and a2, the optimized $\delta(z)$ functions in both cases exhibit large off-resonance at the boundaries ($z = 0$ or 1) to suppress spontaneous dissipation loss. Meanwhile, to obey the adiabatic transfer along the dark eigenmode φ_D ensured by Ω_c and Ω_d, both $\delta(z)$ functions approach near-resonance around the middle of $z = 0.5$, where the probe-to-signal field conversion occurs. The corresponding space-dependent transmission of the probe and signal fields is depicted in Fig. 4b1 and b2. Remarkably, implementations using Protocol III achieve an enhanced CE of approximately 0.469, significantly outperforming Protocol I (0.019) and Protocol II (0.132), highlighting the effectiveness of space-dependent detuning optimization. This results also indicate that the optimization procedure is robust with respect to the choice of functional form, motivating further exploration of different detuning waveforms for experimental implementation.

5 Doppler broadening effect

In the preceding analysis, we set $\delta_p = \delta_c = 0$ to work in the single-photon resonance regime, and leave $\delta = \delta_d$ as the only control parameter for phase-mismatch compensation. We now examine the validity of this assumption at finite temperature by taking account of the Doppler shifts induced by atomic thermal motions.

For a field with frequency ω and wave vector $\mathbf{k}$, the Doppler-shifted frequency experienced by an atom moving with velocity $\mathbf{v}$ is $\omega(\mathbf{v}) = \omega - \mathbf{k} \cdot \mathbf{v}$ [44]. In our two-dimensional geometry, the probe (Ω_p) and signal (Ω_s) fields propagate collinearly along

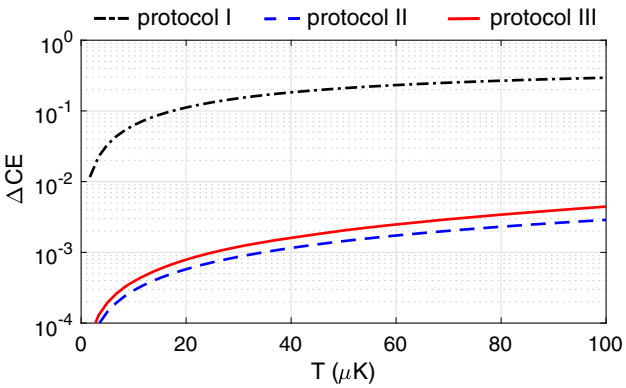

Fig. 5 Effect of Doppler broadening on the CE for the three protocols at $\alpha = 200$ and $\kappa = 5$. The Doppler error ΔCE is plotted versus temperature T. Here, we take $\Gamma = 2\pi \times 6$ MHz, all other parameters are the same as in Fig. 3

the z-axis, while coupling fields (Ω_c, Ω_d) propagate at an angle φ in the xz-plane. We, therefore, consider a two-dimensional Maxwell–Boltzmann velocity distribution

$$P(\mathbf{v}) = \frac{1}{2\pi v_p^2} \exp\left(-\frac{\mathbf{v}^2}{2v_p^2}\right), \tag{21}$$

where $\mathbf{v} \equiv (v_x, v_z)$ and $v_p = \sqrt{k_B T/m}$ is the most probable speed for thermal motion in two dimensions, with m the ^{87}Rb atomic mass. The thermal motion introduces velocity-dependent detunings for each field: $\delta_p^{(v)} = -k_p v_z$, $\delta_c^{(v)} = -k_c(\cos\varphi\, v_z + \sin\varphi\, v_x)$, and $\delta_d^{(v)} = \delta_d - k_d(\cos\varphi\, v_z + \sin\varphi\, v_x)$.

The conversion efficiency at finite temperature can be obtained by solving the Maxwell–Bloch Eq. (11) with the thermally averaged atomic coherences $\langle\rho_{31}\rangle$ and $\langle\rho_{41}\rangle$ over the entire velocity distribution as [45]

$$\langle\rho_{mn}\rangle = \int \rho_{mn}(\mathbf{v})\, P(\mathbf{v})\, d^2\mathbf{v}, \tag{22}$$

where $\rho_{mn}(\mathbf{v})$ is the steady-state solution of the Hamiltonian (2) with the velocity-dependent detunings.

The single-photon Doppler shift $|\delta_p^{(v)}| \sim k_p v_p$ sets the characteristic scale for the inhomogeneous broadening of the $|1\rangle \leftrightarrow |3\rangle$ transition. At $T = 100\ \mu$K, the corresponding Doppler width is about $k_p v_p/(2\pi) \approx 0.125$ MHz, which is much smaller than the excited-state natural linewidth ($\approx 2\pi \times 6$ MHz). The two-photon Doppler shift between the probe and coupling fields is $\delta_p^{(v)} - \delta_c^{(v)} = -(k_p - k_c\cos\varphi)\, v_z - k_c \sin\varphi\, v_x$. For small beam-separation angles ($\varphi \ll 1$), the longitudinal component is suppressed by the near-cancellation $k_p \approx k_c \cos\varphi$, and the residual two-photon detuning is dominated by the transverse term $k_c \sin\varphi\, v_x$, which scales as $\varphi\, k_c v_p$. This partial cancellation of two-photon detuning underlies the robustness of the copropagating Λ-type configuration against Doppler broadening.

To quantify the impact of Doppler broadening on the three protocols, we define the deviation degree, i.e., Doppler error, as

$$\Delta\text{CE} = \text{CE}(T = 0) - \text{CE}(T), \tag{23}$$

Fig. 5 shows ΔCE as a function of temperature for $\alpha = 200$ and $\kappa = 5$. Explicitly, the CE of protocols II and III remains insensitive to T across the entire range, with the error $\Delta\text{CE} < 10^{-2}$ even at $T = 100\mu$K. Whereas for Protocol I, in contrast, CE degrades rapidly suffering from a significant Doppler error as high as $\sim 10^{-1}$. This sharp contrast reflects the role of dark state. In Protocol I, the fixed constant parameters are optimized for a specific set of system parameters. Doppler shifts displace atoms away from this optimized condition, significantly altering the atomic response and CE values. In Protocols II and III, the CE is governed by the adiabatic evolution along the dark state. Importantly, the dark state remains an eigenstate of the system even in the presence of velocity-dependent detunings. Protocol III shows a slightly larger ΔCE than Protocol II. This is because the GA-optimized $\delta(z)$ encodes a precise spatially dependent two-photon detuning profile. Doppler shifts at finite temperature add a velocity-dependent offset to this profile, partially disrupting the compensation. Nevertheless, the absolute CE of Protocol III remains higher than that of Protocol II over the entire temperature range, confirming that the GA-optimized phase-mismatch compensation outperforms the bare dark-state protocol even in the presence of thermal broadening.

Overall, these results demonstrate that Protocols II and III are robust at MOT temperatures ($T \lesssim 100\ \mu$K), exhibiting less than 1% degradation in conversion efficiency.

6 Conclusion

We present a novel scheme to mitigate the detrimental effects of phase-mismatch in a non-resonant FWM system using optimal-control strategy. It is demonstrated that when the two coupling fields are maintained as fixed linear spatial modulations, an optimized

waveform for a single coupling detuning can strongly suppress the spontaneous decay loss from two excited states, leading to a substantial enhancement in the CE even for the large phase-mismatch regime. Our Protocol III with its carefully designed detuning provides superior robustness against variations in mismatch while preserving high-efficiency signal transmission, a key requirement for all-optical quantum information processing such as in frequency conversion involving structured light modes where high efficiency is crucial [46]. These features are expected to significantly relax the technical constraints on phase-matching conditions, motivating further exploration in diverse scenarios [47, 48].

Acknowledgements This work was supported by the National Natural Science Foundation of China (Grants No. 12174106, No. 11474094, No. 12104308, and No. 11104076), the Natural Science Foundation of Chongqing (Grant No. CSTB2024NSCQ-MSX1117), the Shanghai Science and Technology Innovation Project (Grant No. 24LZ1400600), and the Science and Technology Commission of Shanghai Municipality (Grant No. 18ZR1412800). Hamid R. Hamedi gratefully acknowledges the support from the Research Council of Lithuania (LMTLT), agreement No. S-ITP-24-6.

Data availability No external data were used in this research. All data supporting the findings of this study are included within the article.

Declarations

Conflict of interest The authors assert that they do not have any conflict of interest.

Appendix A Deriving the optimal parameters θ_{opt} and δ_{opt} for protocol I

The propagation dynamics of FWM are described by Eq. (12), where the matrix $\mathcal{M}$ encapsulates the coupling and loss mechanisms in the system. This matrix can be decomposed in the Pauli basis as $\mathcal{M} = h_0\mathbb{I} + \Delta\sigma_z + \Omega\sigma_x$, with $\mathbb{I}$ the identity matrix, $\sigma_{x,z}$ the Pauli matrices, and coefficients

$$h_0 = (\zeta + \kappa)/2, \tag{A1a}$$

$$\Delta = -(\zeta \cos 2\theta + \kappa)/2, \tag{A1b}$$

$$\Omega = \zeta \sin 2\theta/2. \tag{A1c}$$

Here, h_0 contributes a global phase and amplitude modulation, Δ acts as an effective detuning, and Ω quantifies the coupling between the probe field Ω_p and the signal field Ω_s. Due to the complex nature of ζ (as defined in the main text), these coefficients are complex, reflecting the non-Hermitian character of the system arising from spontaneous emission loss [49].

Assuming initial conditions $\Omega_p(0) = \Omega_{p0}$ and $\Omega_s(0) = 0$, exact solution of the linear system defined by Eq. (12) is

$$\Omega_s(z) = -i\frac{\Omega}{\tilde{\Omega}}\sin(\tilde{\Omega}z)e^{-ih_0 z}\Omega_{p0}, \tag{A2}$$

where $\tilde{\Omega} = \sqrt{\Delta^2 + \Omega^2}$ represents the effective coupling strength. Then, the expression of CE takes the form

$$\text{CE} = |\frac{\Omega_s(z=1)}{\Omega_{p0}}|^2 = |\frac{\Omega}{\tilde{\Omega}}\sin\tilde{\Omega}|^2 e^{\text{Im}(\zeta)}, \tag{A3}$$

where we have used the relation $|e^{-ih_0}|^2 = e^{\text{Im}(\zeta)}$ and $\text{Im}(\zeta) < 0$ implying overall spontaneous emission loss. Owing to the complexity of ζ, an exact analytical maximization of Eq. (A3) is intractable. We therefore consider the weak spontaneous emission regime, where $|\text{Im}(\zeta)| \ll |\text{Re}(\zeta)|$. In this limit, the imaginary part of ζ is neglected to leading order, and we approximate $\zeta \simeq |\zeta|$. Consequently, Δ and Ω are taken to be effectively real, yielding $\Delta \approx \Delta' \equiv -(|\zeta|\cos 2\theta + \kappa)/2$ and $\Omega \approx \Omega' \equiv (|\zeta|\sin 2\theta)/2$.

To maximize CE, we impose the resonance condition $\Delta' = 0$, which ensures $\Omega/\tilde{\Omega} \sim 1$, and simultaneously set $\Omega' = \pi/2$ to maximize $\sin\tilde{\Omega} \sim 1$. These yield

$$|\zeta|\cos 2\theta_{\text{opt}} = -\kappa, \tag{A4a}$$

$$|\zeta|\sin 2\theta_{\text{opt}} = \pi. \tag{A4b}$$

Dividing Eq.(A4b) by Eq.(A4a) gives $\tan 2\theta_{\text{opt}} = -\pi/\kappa$. Then, θ_{opt} can be expressed as

$$\theta_{\text{opt}} = \frac{\pi}{4} + \frac{1}{2}\arctan(\frac{\kappa}{\pi}). \tag{A5}$$

This expression indicates a deviation from the balanced point $\theta = \pi/4$ for nonzero phase-mismatch κ.

Squaring and adding Eqs.(A4) yields $|\zeta|^2 = \pi^2 + \kappa^2$. Inserting Eq.(A5) into the expression for ζ and solving for δ_{opt} such that $|\zeta| = \sqrt{\pi^2 + \kappa^2}$, we obtain

$$\delta_{\text{opt}} = \frac{\sqrt{\pi^2 + k^2} + k}{2\pi^2}\sqrt{\alpha^2 - 4(\pi^2 + k^2)}. \tag{A6}$$

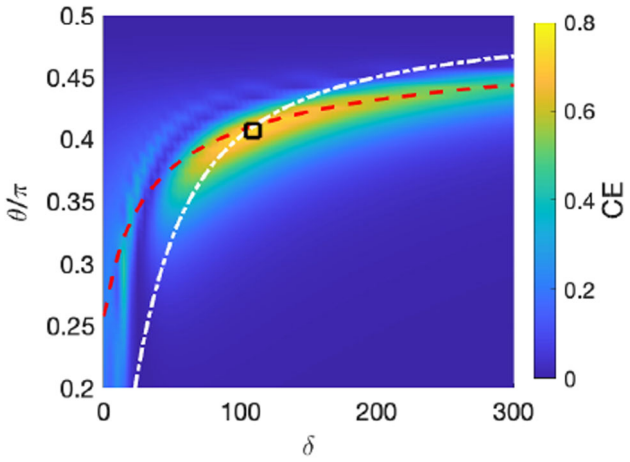

Fig. 6 Contour plot of CE as a function of δ and θ for $\kappa = 5$ and $\alpha = 200$, computed using Eq.(12). The analytical conditions from Eqs. (A4a) (red dashed line) and (A4b) (white dash-dotted line) intersect near the numerical maximum of CE (black square)

The approximation's validity requires $|\mathrm{Re}(\zeta)|/|\mathrm{Im}(\zeta)| \gg 1$, or equivalently $2\delta\cos^2\theta \gg 1$. Substituting the optimal values gives $2\delta_{\mathrm{opt}}\cos^2\theta_{\mathrm{opt}} = \sqrt{\alpha^2/[2(\pi^2+\kappa^2)]} - 2 \gg 1$, which holds when $\alpha^2 \gg 4(\pi^2+\kappa^2)$. In this limit, Eq.(A6) simplifies to

$$\delta_{\mathrm{opt}} \approx \frac{\alpha}{2\pi^2}(\sqrt{\pi^2+k^2}+k). \tag{A7}$$

This regime suppresses spontaneous emission losses via large δ_{opt} while maintaining the required $|\zeta|$ for optimal coupling.

Under these optimal parameters, the maximum CE for phase-mismatch systems is given by

$$\mathrm{CE} \approx \exp\left(-\frac{2(\pi^2+\kappa^2)}{\alpha}\right), \tag{A8}$$

which approaches unity for large optical depth α.

To assess the error introduced by the weak spontaneous emission loss approximation and validate our analytical results, we numerically compute the CE as a function of the control parameters θ and δ for fixed κ. In Fig. 6, the contour plot illustrates the landscape of CE over the parameter space of δ and θ for $\kappa = 5$ and $\alpha = 200$. The analytical optimal conditions Eqs.(A4) converge closely to the region of peak efficiency, confirming the analytical expressions θ_{opt} and δ_{opt} effectively yield the maximum CE.

References

1. Y. Zhang, U. Khadka, B. Anderson, M. Xiao, Temporal and spatial interference between four-wave mixing and six-wave mixing channels. Phys. Rev. Lett. **102**, 013601 (2009)
2. Z. Zhang, F. Wen, J. Che, D. Zhang, C. Li, Y. Zhang, M. Xiao, Dressed gain from the parametrically amplified four-wave mixing process in an atomic vapor. Sci. Rep. **5**, 15058 (2015)
3. M. Bradford, J.-T. Shen, Single-photon frequency conversion by exploiting quantum interference. Phys. Rev. A **85**, 043814 (2012)
4. M.T. Turnbull, P.G. Petrov, C.S. Embrey, A.M. Marino, V. Boyer, Role of the phase-matching condition in nondegenerate four-wave mixing in hot vapors for the generation of squeezed states of light. Phys. Rev. A **88**, 033845 (2013)
5. M. Fleischhauer, A. Imamoglu, J.P. Marangos, Electromagnetically induced transparency: optics in coherent media. Rev. Mod. Phys. **77**, 633 (2005)
6. M.D. Lukin, P.R. Hemmer, M. Löffler, M.O. Scully, Resonant enhancement of parametric processes via radiative interference and induced coherence. Phys. Rev. Lett. **81**, 2675 (1998)
7. M.D. Lukin, S.F. Yelin, M. Fleischhauer, M.O. Scully, Quantum interference effects induced by interacting dark resonances. Phys. Rev. A **60**, 3225 (1999)
8. Y. Niu, R. Li, S. Gong, High efficiency four-wave mixing induced by double-dark resonances in a five-level tripod system. Phys. Rev. A **71**, 043819 (2005)
9. J.-Y. Juo, J.-K. Lin, C.-Y. Cheng, Z.-Y. Liu, I.A. Yu, Y.-F. Chen, Demonstration of spatial-light-modulation-based four-wave mixing in cold atoms. Phys. Rev. A **97**, 053815 (2018)
10. D.A. Braje, V. Balić, S. Goda, G.Y. Yin, S.E. Harris, Frequency mixing using electromagnetically induced transparency in cold atoms. Phys. Rev. Lett. **93**, 183601 (2004)
11. F. Dell'Anno, S. Siena, F. Illuminati, Multiphoton quantum optics and quantum state engineering. Phys. Rep. **428**, 53 (2006)
12. Y. Zhao, Y. Yang, H.-B. Sun, Nonlinear meta-optics towards applications. PhotoniX **2**, 3 (2021)
13. H. Suchowski, D. Oron, A. Arie, Y. Silberberg, Geometrical representation of sum frequency generation and adiabatic frequency conversion. Phys. Rev. A **78**, 063821 (2008)
14. L. Deng, M. Kozuma, E.W. Hagley, M.G. Payne, Opening optical four-wave mixing channels with giant enhancement using ultraslow pump waves. Phys. Rev. Lett. **88**, 143902 (2002)
15. M. Johnsson, E. Korsunsky, M. Fleischhauer, Eliminating nonlinear phase mismatch in resonantly enhanced four-wave mixing. Optics Commun. **212**, 335 (2002)
16. A.S. Zibrov, M.D. Lukin, M.O. Scully, Nondegenerate parametric self-oscillation via multiwave mixing in coherent atomic media. Phys. Rev. Lett. **83**, 4049 (1999)
17. H. Kang, G. Hernandez, Y. Zhu, Slow-light six-wave mixing at low light intensities. Phys. Rev. Lett. **93**, 073601 (2004)

18. J.P. Lopez, A.M.G. Melo, D. Felinto, J.W.R. Tabosa, Observation of giant gain and coupled parametric oscillations between four optical channels in cascaded four-wave mixing. Phys. Rev. A **100**, 023839 (2019)
19. J. Wu, M. Guo, H. Zhou, J. Liu, J. Li, J. Zhang, Experimental realization of efficient nondegenerate four-wave mixing in cesium atoms. Opt. Express **30**, 12576 (2022)
20. M. Jain, H. Xia, G.Y. Yin, A.J. Merriam, S.E. Harris, Efficient nonlinear frequency conversion with maximal atomic coherence. Phys. Rev. Lett. **77**, 4326 (1996)
21. R. Li, S. Li, D. Yu, J. Qian, W. Zhang, Optimal model for fewer-qubit cnot gates with Rydberg atoms. Phys. Rev. Appl. **17**, 024014 (2022)
22. D. Stefanatos, A. Smponias, H.R. Hamedi, E. Paspalakis, Ultimate conversion efficiency bound for the forward double-Λ atom-light coupling scheme. Opt. Lett. **45**, 6090 (2020)
23. K. Li, J. Wen, Y. Cai, S.V. Ghamsari, C. Li, F. Li, Z. Zhang, Y. Zhang, M. Xiao, Direct generation of time-energy-entangled W triphotons in atomic vapor. Sci. Adv. **10**, 3199 (2024)
24. R.F. Offer, A. Daffurn, E. Riis, P.F. Griffin, A.S. Arnold, S. Franke-Arnold, Gouy phase-matched angular and radial mode conversion in four-wave mixing. Phys. Rev. A **103**, 021502 (2021)
25. G. Wang, L. Cen, Y. Qu, Y. Xue, J.-H. Wu, J.-Y. Gao, Intensity-dependent effects on four-wave mixing based on electromagnetically induced transparency. Opt. Express **19**, 21614 (2011)
26. R.W. Boyd, *Nonlinear Optics*, 4th edn. (Academic Press, London, 2020)
27. L. Deng, M.G. Payne, Inhibiting the onset of the three-photon destructive interference in ultraslow propagation-enhanced four-wave mixing with dual induced transparency. Phys. Rev. Lett. **91**, 243902 (2003)
28. E. Braaten, H.-W. Hammer, G.P. Lepage, Lindblad equation for the inelastic loss of ultracold atoms. Phys. Rev. A **95**, 012708 (2017)
29. J. Qiu, Z. Wang, D. Ding, Z. Huang, B. Yu, Control of space-dependent four-wave mixing in a four-level atomic system. Phys. Rev. A **102**, 033516 (2020)
30. H.-M. Zhao, X.-J. Zhang, D.-D. Zheng, J.-H. Wu, Optimization of narrowband photon pair generation in doppler-broadened atomic vapors. Phys. Rev. A **113**, 043702 (2026)
31. Y. Jiang, Y. Mei, Y. Zuo, Y. Zhai, J. Li, J. Wen, S. Du, Anti-parity-time symmetric optical four-wave mixing in cold atoms. Phys. Rev. Lett. **123**, 193604 (2019)
32. M.O. Scully, M.S. Zubairy, *Quantum Optics* (Cambridge University Press, Cambridge, England, 1997)
33. H.R. Hamedi, J. Ruseckas, G. Juzeliūnas, Exchange of optical vortices using an electromagnetically-induced-transparency-based four-wave-mixing setup. Phys. Rev. A **98**, 013840 (2018)
34. C. Meng, T. Shui, W.-X. Yang, Coherent transfer of optical vortices via backward four-wave mixing in a double-Λ atomic system. Phys. Rev. A **107**, 053712 (2023)
35. C.-Y. Cheng, Z.-Y. Liu, P.-S. Hu, T.-N. Wang, C.-Y. Chien, J.-K. Lin, J.-Y. Juo, J.-S. Shiu, I.A. Yu, Y.-C. Chen, Y.-F. Chen, Efficient frequency conversion based on resonant four-wave mixing. Opt. Lett. **46**, 681 (2021)
36. X. Ding, D. Heberle, K. Harrington, N. Flemens, W.-Z. Chang, T.A. Birks, J. Moses, Observation of rapid adiabatic passage in optical four-wave mixing. Phys. Rev. Lett. **124**, 153902 (2020)
37. G. Li, Y. Geng, X. Pei, J. Wu, X. Lin, D. Yan, H. Zhang, H. Yang, Phase and detuning control of the unidirectional reflection amplification based on the broken spatial symmetry. Opt. Express **32**, 12839 (2024)
38. C. Hang, G. Huang, V.V. Konotop, $\mathcal{PT}$ symmetry with a system of three-level atoms. Phys. Rev. Lett. **110**, 083604 (2013)
39. M. Hosseini, B.M. Sparkes, G. Campbell, P.K. Lam, B.C. Buchler, High efficiency coherent optical memory with warm rubidium vapour. Nat. Commun. **2**, 174 (2011)
40. D. Daems, A. Ruschhaupt, D. Sugny, S. Guérin, Robust quantum control by a single-shot shaped pulse. Phys. Rev. Lett. **111**, 050404 (2013)
41. W. Ketterle, K.B. Davis, M.A. Joffe, A. Martin, D.E. Pritchard, High densities of cold atoms in a dark spontaneous-force optical trap. Phys. Rev. Lett. **70**, 2253 (1993)
42. J. Geng, G.T. Campbell, J. Bernu, D.B. Higginbottom, B.M. Sparkes, S.M. Assad, W.P. Zhang, N.P. Robins, P.K. Lam, B.C. Buchler, Electromagnetically induced transparency and four-wave mixing in a cold atomic ensemble with large optical depth. New J. Phys. **16**, 113053 (2014)
43. Y. Sun, P. Xu, P.-X. Chen, L. Liu, Controlled phase gate protocol for neutral atoms via off-resonant modulated driving. Phys. Rev. Appl. **13**, 024059 (2020)
44. H.-M. Zhao, X.-J. Zhang, D.-D. Zheng, J.-H. Wu, Optimization of narrowband photon pair generation in doppler-broadened atomic vapors. Phys. Rev. A **113**, 043702 (2026)
45. A. Leszczyński, M. Parniak, W. Wasilewski, Phase matching alters spatial multiphoton processes in dense atomic ensembles. Opt. Express **25**, 284 (2017)
46. R.F. Offer, D. Stulga, E. Riis, S. Franke-Arnold, A.S. Arnold, Spiral bandwidth of four-wave mixing in Rb vapour. Commun. Phys. **1**, 84 (2018)
47. Z.-X. Chen, Y.-G. Peng, Z.-G. Chen, Y. Liu, P. Chen, X.-F. Zhu, Y.-Q. Lu, Robust temporal adiabatic passage with perfect frequency conversion between detuned acoustic cavities. Nat. Commun. **15**, 1478 (2024)
48. K. Katamadze, A. Romanova, D. Chupakhin, A. Pashchenko, S. Kulik, Broadband biphoton source for quantum optical coherence tomography based on a michelson interferometer. Phys. Rev. Appl. **23**, 014076 (2025)
49. I. Tsiamis, O. Kyriienko, A.S. Sørensen, Continuous-wave quantum light control via engineered Rydberg-induced dephasing. Phys. Rev. A **113**, 013710 (2026)